

Fluid mixing and the deep biosphere of a fossil Lost City-type hydrothermal system at the Iberia Margin

Frieder Klein^{a,1}, Susan E. Humphris^b, Weifu Guo^b, Florence Schubotz^c, Esther M. Schwarzenbach^d, and William D. Orsi^a

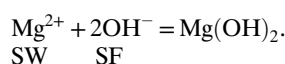
^aDepartment of Marine Chemistry and Geochemistry, Woods Hole Oceanographic Institution, Woods Hole, MA 02543; ^bDepartment of Geology and Geophysics, Woods Hole Oceanographic Institution, Woods Hole, MA 02543; ^cDepartment of Geosciences and Center for Marine Environmental Sciences, University of Bremen, 28334 Bremen, Germany; and ^dDepartment of Geosciences, Virginia Polytechnic Institute and State University, Blacksburg, VA 24061

Edited by David M. Karl, University of Hawaii, Honolulu, HI, and approved August 4, 2015 (received for review March 7, 2015)

Subseafloor mixing of reduced hydrothermal fluids with seawater is believed to provide the energy and substrates needed to support deep chemolithoautotrophic life in the hydrated oceanic mantle (i.e., serpentinite). However, geosphere-biosphere interactions in serpentinite-hosted subseafloor mixing zones remain poorly constrained. Here we examine fossil microbial communities and fluid mixing processes in the subseafloor of a Cretaceous Lost City-type hydrothermal system at the magma-poor passive Iberia Margin (Ocean Drilling Program Leg 149, Hole 897D). Brucite–calcite mineral assemblages precipitated from mixed fluids ca. 65 m below the Cretaceous paleo-seafloor at temperatures of 31.7 ± 4.3 °C within steep chemical gradients between weathered, carbonate-rich serpentinite breccia and serpentinite. Mixing of oxidized seawater and strongly reducing hydrothermal fluid at moderate temperatures created conditions capable of supporting microbial activity. Dense microbial colonies are fossilized in brucite–calcite veins that are strongly enriched in organic carbon (up to 0.5 wt.% of the total carbon) but depleted in ^{13}C ($\delta^{13}\text{C}_{\text{TOC}} = -19.4\%$). We detected a combination of bacterial diether lipid biomarkers, archaeol, and archaeal tetraethers analogous to those found in carbonate chimneys at the active Lost City hydrothermal field. The exposure of mantle rocks to seawater during the breakup of Pangaea fueled chemolithoautotrophic microbial communities at the Iberia Margin, possibly before the onset of seafloor spreading. Lost City-type serpentinization systems have been discovered at midocean ridges, in forearc settings of subduction zones, and at continental margins. It appears that, wherever they occur, they can support microbial life, even in deep subseafloor environments.

serpentinization | microfossils | lipid biomarkers | brucite–calcite | passive margin

Serpentinized mantle rocks constitute a major component of oceanic plates, subduction zones, and passive margins. Serpentinization systems have existed throughout most of Earth's history, and it has been suggested that mixing of serpentinization fluids with Archean seawater produced conditions conducive to abiotic synthesis and the emergence of life on Earth (1). The Lost City hydrothermal field, located ~15 km off the Mid-Atlantic Ridge axis at 30°N (2–4), represents the archetype of low-temperature seafloor serpentinization systems at slow-spreading midocean ridges and serves as an excellent present-day analog to fossil serpentinite-hosted hydrothermal systems in such environments. Lost City vents warm (≤ 91 °C), high-pH (9–11) fluids enriched in dissolved calcium, H_2 , CH_4 , formate, and other short-chain hydrocarbons (2, 5, 6). In contrast to high-temperature black smoker-type chimneys consisting of Cu–Fe sulfides, the Lost City chimneys are composed of brucite and calcium carbonate (aragonite, calcite), which form when serpentinization fluids (SF) mix with seawater (SW) (7),



Nascent Lost City chimneys are dominated by aragonite and brucite, whereas older structures are dominated by calcite. During

aging, brucite undersaturated in seawater dissolves and aragonite recrystallizes to calcite (7).

Actively venting chimneys host a microbial community with a relatively high proportion of methanogenic archaea (the Lost City Methanosarcinales), methanotrophic bacteria, and sulfur-oxidizing bacteria, whereas typical sulfate-reducing bacteria are rare (8–10). Geochemical evidence for significant microbial sulfate reduction in basement lithologies and distinct microbial communities in Lost City vent fluids and chimneys suggest that subsurface communities may be different from those in chimney walls (8, 9, 11). The lack of modern seawater bicarbonate and low $\text{CO}_2/{}^3\text{He}$ in Lost City fluids clearly indicate bicarbonate removal before venting, but it remains unclear if bicarbonate removal occurred by “dark” microbial carbon fixation in a serpentinization-fueled deep biosphere, by carbonate precipitation, or both (12).

Other active and fossil seafloor hydrothermal systems similar to Lost City exist in a range of seafloor environments, including the Mid-Atlantic Ridge (13), New Caledonia (14), and the Mariana forearc (15, 16). *Bathymodiolus* mussels are, in some places, associated with these systems, suggesting that active serpentinization is supporting not only microbial chemosynthetic ecosystems but also macrofaunal communities (16). However, biological processes in the subseafloor of these Lost City-type systems are poorly understood.

Serpentinization at Magma-Poor Continental Margins

The breakup of (super)continents exposes large volumes, on the order of thousands of cubic kilometers (17), of mantle peridotite to seawater, making magma-poor continental margins a prime

Significance

We provide biogeochemical, micropaleontological, and petrological constraints on a subseafloor habitat at the passive Iberia Margin, where mixing of reduced hydrothermal serpentinization fluids with oxic seawater provided the energy and substrates for metabolic reactions. This mixing zone was inhabited by bacteria and archaea and is comparable to the active Lost City hydrothermal field at the Mid-Atlantic Ridge. Our results highlight the potential of magma-poor passive margins to host Lost City-type hydrothermal systems that support microbial activity in subseafloor environments. Because equivalent systems have likely existed throughout most of Earth's history in a wide range of oceanic environments, fluid mixing may have provided the substrates and energy to support a unique subseafloor community of microorganisms over geological timescales.

Author contributions: F.K. designed research; F.K., W.G., F.S., and E.M.S. performed research; F.K., W.G., F.S., and E.M.S. contributed new reagents/analytic tools; F.K., S.E.H., W.G., F.S., E.M.S., and W.D.O. analyzed data; and F.K., S.E.H., W.G., F.S., E.M.S., and W.D.O. wrote the paper.

The authors declare no conflict of interest.

This article is a PNAS Direct Submission.

¹To whom correspondence should be addressed. Email: fklein@whoi.edu.

This article contains supporting information online at www.pnas.org/lookup/suppl/doi:10.1073/pnas.1504674112/-DCSupplemental.

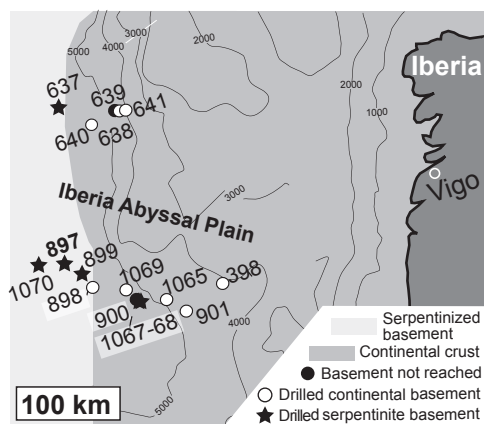


Fig. 1. Simplified geological map of the Iberia Margin showing the localities of drill sites from Ocean Drilling Program Legs 103, 149, and 173. Samples analyzed in this study are from Site 897. Interpretation of geological units is based on drilling results and geophysical surveys (drill site locations and geological interpretation from ref. 60).

target area to search for Lost City-type hydrothermal activity. The archetypal example of magma-poor rifted margins, the Iberia Margin, has been examined by seafloor drilling and geophysical studies (Fig. 1). The ocean–continent transition zone (OCT) at the Iberia Margin is *ca.* 40–170 km wide and is chiefly composed of altered mantle rocks (18). Serpentinization took place due to seawater influx during rifting along numerous faults that have brecciated the uppermost ~1 km (19). Seismic imaging tentatively suggests that the exhumed mantle is ~25–100% serpentinized to ~4 km depth. A deeper section with seismic velocities of 7.3–7.9 km/s can be interpreted as partly (<25%) serpentinized peridotite, with higher extents of serpentinization along deep-reaching fault planes (19). The Mohorovičić discontinuity of the southern Iberia Abyssal Plain is interpreted as a gradual transition from partly serpentinized peridotite to unaltered peridotite with a seismic velocity of 8 km/s (19). Laboratory experiments suggest that serpentinization of such large volumes lasted at least a few million years (20). The conjugate Newfoundland Margin likely exposed similar volumes of mantle peridotite to seawater (21), as did other magma-poor passive margins, such as the South Australian Margin and the West Greenland–Labrador conjugate margins (22).

Serpentinization Beneath the Iberia Abyssal Plain

During Ocean Drilling Program Leg 149, Hole 897D penetrated the OCT beneath the Southern Iberia Abyssal Plain to 837.2 m depth. The oldest sediment, cored at 693.8 m below the seafloor (mbsf), was deposited during the Lower Cretaceous when, or shortly before, seafloor spreading initiated the separation of North America and Iberia (23). The sediment–basement interface at this depth represents the approximate Lower Cretaceous (~Aptian) paleo-seafloor; however, because the lowermost sedimentary unit is interpreted as a series of mass flows (24), it remains unclear how thick the sediment cover was during serpentinization. A comparison of $^{87}\text{Sr}/^{86}\text{Sr}$ isotopes in calcite veins in serpentinite with the Sr isotopic curve for Cretaceous seawater reveals that the inferred ages are consistent with the timing inferred from sediment stratigraphy (25).

Basement lithologies of Hole 897D can be divided into an upper ophalcalcite section (brecciated serpentinite cut by calcite veins) and a deeper serpentinite section that is largely devoid of carbonate veins (26). The boundary between these sections is at 65 m below the basement–sediment interface (26). Oxygen isotope thermometry reveals serpentinization temperatures of *ca.* 130–250 °C at Site 897 (27–29). Serpentinization went to completion

in most recovered samples and produced serpentine (lizardite + chrysotile), brucite, minor chlorite, and traces of magnetite and other opaque minerals. Thermodynamic constraints and hydrothermal experiments suggest that serpentinization fluids associated with this assemblage are alkaline, depleted in dissolved inorganic carbon ($\Sigma\text{CO}_2 = \text{CO}_2, \text{HCO}_3^-, \text{CO}_3^{2-}$), SiO_2 , and Mg but enriched in dissolved Ca and H_2 compared with seawater (30, 31). Accessory opaque minerals include valleriite, pentlandite, millerite, chalcopyrite, siegenite, polydymite, and pyrite, in addition to the relict Ni–Fe alloy awaruite and native Cu (26). Awaruite, armored by magnetite from dissolution, indicates strongly reducing conditions and low sulfur fugacities during the main stages of active serpentinization (26). Later, conditions became less reducing and sulfur fugacities increased, as indicated by sulfur-rich sulfides such as millerite and polydymite. Opaque minerals in ophalcalcite, including pyrite, millerite (26), hematite, and goethite, record oxidizing conditions due to prolonged ingress of cold, oxidized seawater, which also led to precipitation of clay minerals and quartz at the expense of serpentine at temperatures ≤ 100 °C (32). The mineralogical differences between the upper ophalcalcite section and the deeper serpentinite section provide evidence for strong chemical gradients in pH, $f\text{O}_2$, ΣCO_2 , and SO_4^{2-} over a short interval between ~60 m and 70 m below the sediment–basement interface.

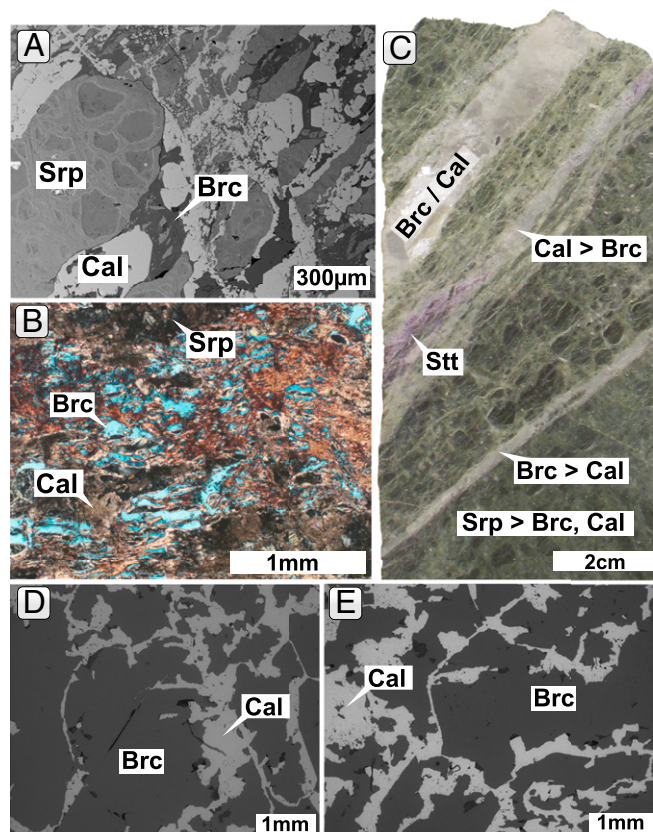


Fig. 2. (A) Thin section back-scattered electron (BSE) image showing the brecciated serpentinite host, mainly composed of serpentine (Srp) cemented by calcite (Cal) and brucite (Brc). (B) Thin section photomicrograph of brucite–carbonate altered serpentinite host in crossed polarized light. (C) Core photograph showing the brecciated and veined host. The pink mineral is stichtite (Stt), a hydrous Mg–Cr carbonate that formed at the expense of Cr spinel and brucite. The large vein is composed of brucite and calcite in approximately equal amounts, whereas brucite/calcite ratios in smaller veins vary. (D and E) BSE images of calcite in a feathery texture together with large subhedral brucite crystals similar to chimney material from the Lost City hydrothermal field (7).

The present study examined this transition zone in detail to further illuminate geochemical processes and their potential to support microbial life.

Lost City-Type Brucite–Calcite Assemblages in Hole 897D

During systematic examination of drill core samples from Hole 897D, we discovered millimeter- to centimeter-sized brucite–calcite veins crosscutting the serpentinite host at angles of 40–50° (Fig. 2) at 758 mbsf (65 m below the basement–sediment interface), right at the boundary between opicalcite and serpentinite. Well-developed crystal habits of brucite and calcite point to precipitation from percolating solutions in open fractures, possibly during or after tectonic shearing of the serpentinite (Fig. 2). Analogous to Lost City chimneys, it seems possible that aragonite coprecipitated first with brucite, and subsequently recrystallized to calcite. However, the low Mg/Ca ratio of seawater during the Lower Cretaceous likely favored the direct formation of calcite (33). Neither brucite nor calcite shows any compositional or optical zonation, indicating that fluid compositions remained relatively constant during crystal growth. In many instances, dendritic calcite forms intergrowths with brucite (Fig. 2 D and E), similar to fragile brucite–carbonate intergrowths found in Lost City chimneys (7). Vein brucite associated with calcite is of virtually pure endmember composition (Table S1). Bulk chemical analysis of chimney samples suggests that brucite at Lost City is also Fe-poor (7), consistent with the metal-poor nature of Lost City fluids (3, 34). For comparison, brucite formed at the expense of olivine in serpentinitized peridotite from the Iberia Margin is intergrown with serpentine and strongly enriched in Fe (35). Calcite associated with brucite is of near-endmember composition with only trace contents of Mg, Mn, and Fe (<0.05 wt%, Table S1; cf. ref. 7).

The serpentinitized host is heavily brecciated with individual clasts, mainly composed of serpentinite in mesh or hourglass texture, being cemented by vein calcite and brucite (Fig. 2 A–C). Calcite and brucite deposition clearly postdated serpentinitization in this depth interval, suggesting that hydrothermal fluids were sourced in deeper basement levels.

Carbon Geochemistry of a Suboceanic Mixing Zone

The contact at 65 m below the sediment–basement interface between opicalcite and serpentinite marks a sharp transition in carbon geochemistry (Fig. 3) (32). Contents of total inorganic carbon (TIC) are high (1.2–9.6 wt.%) above the contact, whereas the total carbon (TC) $\delta^{13}\text{C}$ ranges between +1.2‰ and –4.3‰. Contents of total organic carbon (TOC) are low in this section. In contrast, below the contact, contents of TOC are up to 0.4 wt.%, making up more than 80% of the TC, and $\delta^{13}\text{C}_{\text{TC}}$ is strongly depleted (29). The brucite–calcite veins analyzed in this study have TC (4.87 ± 0.19 wt.%, $\delta^{13}\text{C}_{\text{TC}} = -1.6$ ‰) and TIC (4.40 ± 0.06 wt.%, $\delta^{13}\text{C}_{\text{TIC}} = -0.3 \pm 0.06$ ‰, $\delta^{18}\text{O}_{\text{TIC}} = -1.7 \pm 0.19$ ‰) contents and isotope compositions consistent with opicalcite in the upper drill core section. In contrast, TOC is strongly enriched in these veins, with contents of 0.49 ± 0.01 wt.%, which is even higher than TOC contents of serpentinite from the lower section (Fig. 3). Although $\delta^{13}\text{C}_{\text{TOC}} = -19.4$ ‰ is somewhat less depleted than in other samples from Hole 897D, it is almost identical to that of carbonate samples from fissures in the serpentinite bedrock at Lost City (36, 37).

It seems likely that organic carbon was introduced by seawater into the deeper sections of the basement; however, this would not explain the enrichment of organic carbon at the contact between opicalcite and serpentinite or in some places within the lower serpentinite section.

Clumped isotope analysis of vein calcites intergrown with brucite yields Δ_{47} values of 0.670 ± 0.019 ‰ ($n = 3$, mean $\pm 1\sigma$ SE), suggesting they formed at 31.7 ± 4.3 °C from a fluid with $\delta^{18}\text{O}$ values of 1.2 ± 0.9 ‰ [Vienna standard mean ocean water, VSMOW (38–40)]. This temperature range is consistent with

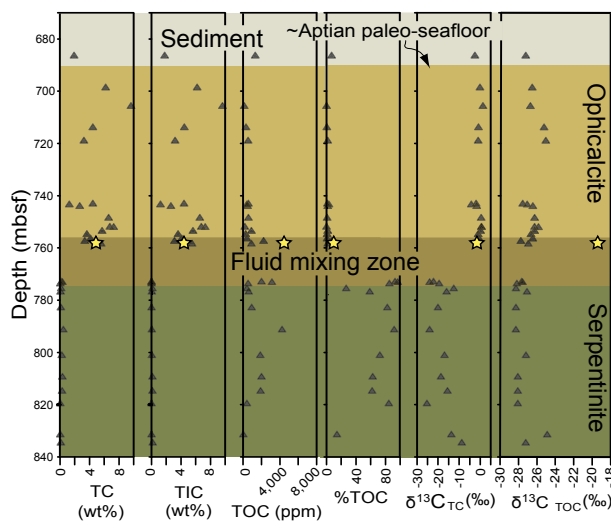


Fig. 3. Carbon geochemistry of samples from drill cores recovered from Hole 897D during ODP Leg 149 as a function of depth in meters below the seafloor (mbsf). The uppermost section consists of Lower Cretaceous (~Aptian) sediment overlying the igneous basement. The uppermost part of the igneous basement consists of opicalcite, i.e., brecciated and strongly oxidized serpentinite cut by calcite veins. The fluid mixing zone features brucite–calcite veins and coincides with a shear zone between opicalcite and serpentinite. Yellow stars indicate measured values of brucite–calcite samples. Note the differences in carbon geochemistry between the opicalcite and serpentinite sections. Adapted from ref. 29, with permission from Elsevier.

previous estimates for carbonate precipitation temperatures at Hole 897D (21–31 °C) (29). Moreover, the calculated isotopic composition of the fluid is within the range of the measured isotopic composition of Lost City vent fluids [0.5–2‰ (3)].

In Situ Biomass Production

Thermodynamic predictions provide valuable constraints on possible metabolic (catabolic and anabolic) reactions in hydrothermal mixing zones. Amend et al. (41) calculated that hydrogen oxidation in peridotite-hosted hydrothermal systems yields the most catabolic energy at low to moderate temperatures (<~45 °C) and seawater : hydrothermal fluid mixing ratios of >10. Other aerobic and anaerobic reactions, including methane oxidation, sulfate reduction, and methanogenesis, are exergonic under these conditions but, energetically, less favorable than hydrogen oxidation. Similar to catabolic reactions, anabolic reactions are most favorable at high seawater : hydrothermal fluid mixing ratios and temperatures ≤ 32 °C in peridotite-hosted hydrothermal systems with energy yields of ~900 J per gram of dry cell mass (41). Assuming serpentinitization fluids beneath the Iberia Abyssal Plain had a temperature of ~150–250 °C as indicated from oxygen isotope thermometry, and bottom seawater was ~2 °C, we calculate isenthalpic seawater : hydrothermal fluid mixing ratios of ~3–15 to yield carbonate precipitation temperatures of 20–40 °C. Hence, the energy landscape was likely favorable for a range of aerobic and anaerobic reactions across the mixing zone. We suggest that in situ production of microbial biomass fueled by fluid mixing represents the most plausible explanation for the measured enrichments in organic carbon (Fig. 3).

Microfossil Inclusions

Transmitted light and electron microscopy of freshly broken brucite–calcite veins (sample 897D-17R6, 0–5 cm) revealed abundant round to rod-shaped inclusions, ca. 2–200 μm in diameter (Fig. 4 A–D), that bear a striking resemblance to microbial microcolonies, i.e., micrometer-scale clusters of physically

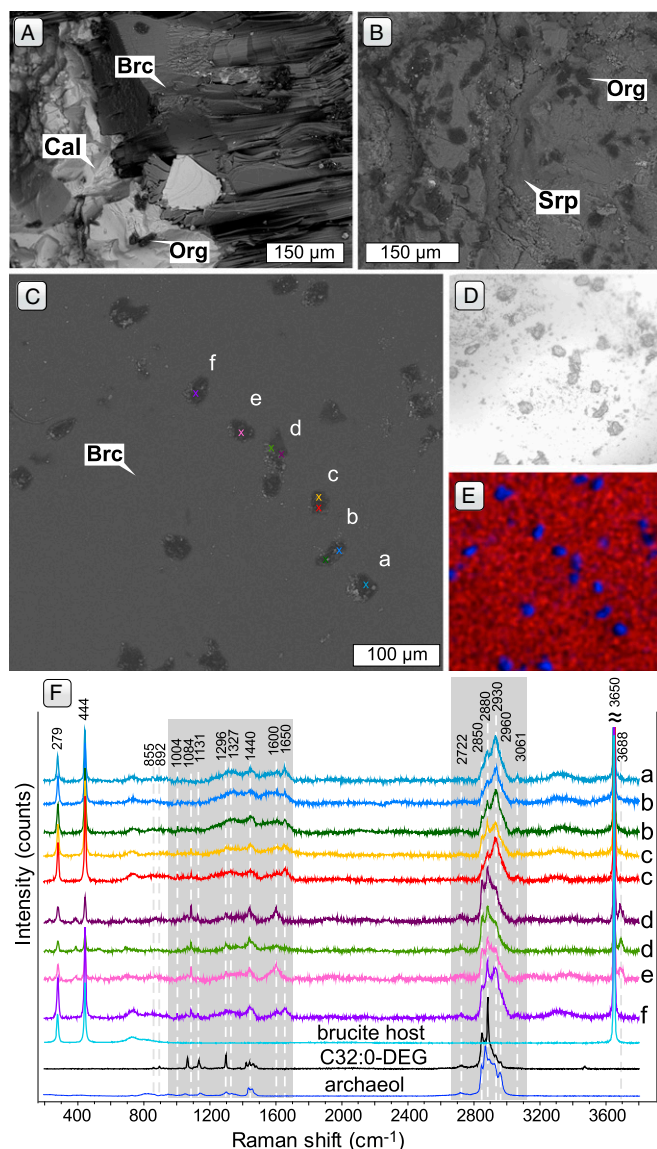


Fig. 4. Examples of fossilized colonies of microorganisms in sample 897D-17R6, 0–5 cm. (A) BSE image of concretions of organic matter (Org) interpreted to be fossil microbial microcolonies in calcite (Cal) and sheets of brucite (Brc). (B) BSE image of concretions of organic matter interpreted to be fossil microbial microcolonies at a contact between a brucite–calcite vein and the serpentinite host. (C) BSE image of microcolonies in brucite. Negative crystal shapes of brucite are visible in some inclusions. Color-coded crosses and labels refer to Raman spectra shown in F. (D) Optical photomicrograph of same microcolonies as shown in C and E. (E) Element map of microcolonies, carbon (blue) and magnesium (red). (F) Raman spectra of brucite-hosted microcolonies illustrated in C–E. Raman spectra of the brucite host, and 1,2-Di-O-hexadecyl-rac-glycerol (C32:0-DEG, $\geq 99\%$) and 1,2-Di-O-phytyl-sn-glycerol (archaeol, $>99\%$) lipid standards are shown for comparison.

adjacent microbial cells (42). Some inclusions show negative crystal shapes evidencing entrapment during crystal growth (Fig. 4C). Energy dispersive element mapping suggests that these inclusions are chiefly composed of carbonaceous matter (Fig. 4E).

Microfossil inclusions are found in brucite and calcite, but Raman spectra of such inclusions were exclusively collected in brucite because of its lower background and nominally carbon-free nature. Brucite yields strong bands at 279 cm^{-1} , 444 cm^{-1} , and $3,650\text{ cm}^{-1}$ and a weak band at 725 cm^{-1} (Fig. 4F), which is

consistent with band assignments from reference spectra (43). The Raman spectra acquired from the microfossil inclusions contain prominent vibrational modes in the $\sim 2,800$ – $3,100\text{ cm}^{-1}$ and $\sim 1,000$ and $1,650\text{ cm}^{-1}$ ranges (Fig. 4F). These bands can be assigned to the C–H, $-\text{CH}_2$, and $-\text{CH}_3$ functional groups in lipids and amino acid side chains of proteins and carbohydrates, and amide I bonds in proteins (44–46) (Table S2).

Microbial Signatures

Lipid biomarkers were extracted from homogenized and crushed brucite–calcite veins (sample 897D-17R6, 0–2 cm) and subjected to multiple reaction monitoring (MRM) experiments with HPLC triple quadrupole MS to screen the sample for fossilized forms of characteristic Lost City-type membrane lipid biomarkers as reported previously (47, 48). MRM experiments revealed the presence of a series of nonisoprenoidal dialkylglycerol diether (DEG) lipids of bacterial origin, with varying chain lengths from C30:0 to C34:0 representing different mixtures of C15 to C18 hydrocarbon chains (Fig. 5). The same compounds represent the predominant lipid type in Lost City hydrothermal vent chimneys in their intact form with sugars as head groups (47). *Desulfotomaculum* and *Clostridium*, candidate sulfate-reducing bacteria detected at Lost City, have been suggested as potential source organisms for these compounds (47). In addition to bacterial DEG lipids (amounting to $2,370\text{ pg}\cdot\text{g}^{-1}$), quantifiable amounts of archaeol (13 $\text{pg}\cdot\text{g}^{-1}$) and acyclic glycerol dibiphytanyl glycerol tetraether lipids (GDGT-0, 13 $\text{pg}\cdot\text{g}^{-1}$) were detected in brucite–calcite veins from the Iberia Margin. The same lipids are present in Lost City chimneys and are attributed to methanogenic archaea, likely those belonging to the Methanosarcinales (47, 48). Methanosarcinales dominate microbial communities harbored

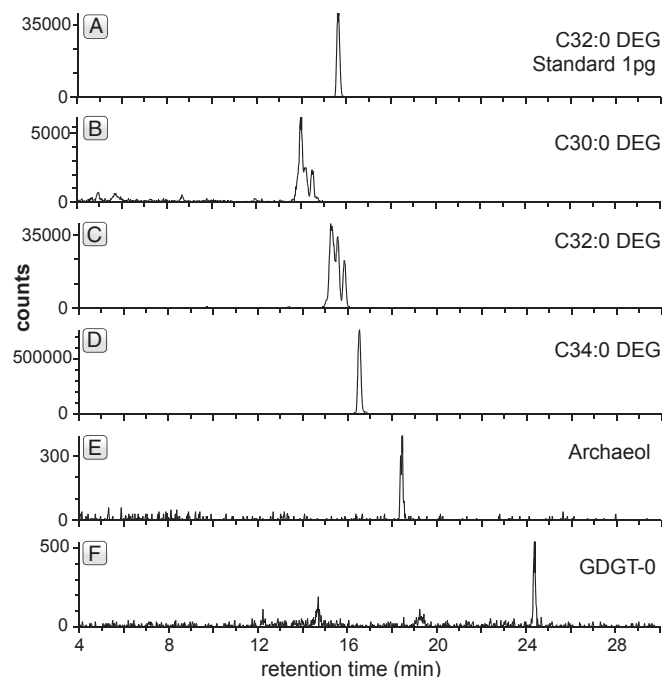


Fig. 5. Representative HPLC-ESI-MS chromatograms of organic compounds detected in MRM experiments: (A) C32:0 nonisoprenoidal diether glycerol (DEG) lipid standard, having two C16 hydrocarbon side chains; (B–D) nonisoprenoidal bacterial DEG lipids with different side chains detected in sample 897D-17R6 0–2 cm. Multiple peaks are likely due to different mixtures of hydrocarbon side chains or methylations in the hydrocarbon chains. (E and F) Isoprenoidal archaeal ether lipids detected in sample 897D-17R6 0–2 cm (GDGT-0, acyclic glycerol dibiphytanyl glycerol tetraether). Bacterial lipids outnumber archaeal lipids as in mixed fluid environments at Lost City (cf. ref. 49).

within the inner parts of Lost City chimneys that are completely immersed in hydrothermal fluid, whereas bacteria dominate outer areas that are exposed to a mixture of hydrothermal fluid and seawater (49). Bacteria were also likely more abundant than archaea in the mixing zone at the Iberia Margin, as suggested by the relative abundances of lipid biomarkers.

The combination of membrane lipid biomarkers detected in this study has been found in only two other seafloor environments: cold seep systems, including mud volcanoes, and at the Lost City hydrothermal field (47, 48, 50). Therefore, it seems very unlikely that these lipids are due to contamination during sample storage at the core repository or sampling.

Serpentinization and Subseafloor Microbial Activity

Seafloor serpentinization systems have existed throughout most of Earth's history (51). Serpentinization is currently taking place in the shallow forearc of subduction zones, along ultraslow-, slow-, and fast-spreading midocean ridges where oceanic mantle is exposed to water (52–55). Whether serpentinization is currently taking place along passive margins is unclear, but it certainly occurred in the geological past, as shown in the present study. Biological communities associated with hydrothermal systems exploit and likely follow the chemical energy they provide, independent of the geotectonic setting where serpentinization occurs. The environmental conditions in subseafloor serpentinizing systems can be extremely challenging for microorganisms due to the high pH and limited availability of electron acceptors and nutrients (10). However, our study demonstrates what theoretical studies predicted earlier (41, 56, 57): Subseafloor mixing zones represent niches for chemolithoautotrophic life in the oceanic mantle.

Methods

Thin sections of samples from Ocean Drilling Program Leg 149 Hole 897D, core 17R6, were prepared at High Mesa Petrographics (Los Alamos, NM). Thin sections were examined with a Zeiss Axio Imager 2 petrographic microscope in transmitted and reflected light. Back-scattered electron images of thin sections and rock chips were collected with a Hitachi TM3000 scanning electron microscope. Mineral compositions were quantified with a JEOL JXA-8530F HyperProbe Field-Emission Electron Probe Microanalyzer (Yale University) operated at 15 kV acceleration voltage and 20-nA beam current. The beam was set to 5–15 μm in diameter to avoid beam damage. Counting times for all elements were 20 s, except for F, which was analyzed for 120 s. Thin sections and rock chips were analyzed with a Horiba LabRAM HR confocal Raman spectrometer equipped with a 17-mW 633-nm HeNe laser, a 25-mW 473-nm diode-pumped solid state laser, an astigmatic flat field spectrograph with a focal length of 800 mm, and a multichannel air-cooled (–70 °C) CCD detector. Individual spectra were recorded using Olympus MPlan N objectives with 50 \times and 100 \times magnification and a numerical aperture of 0.75 and 0.9, respectively. Gratings with 600 grooves per millimeter and 1,800 grooves per millimeter were used for identification of minerals and organic substances. A confocal hole diameter of 100 μm was chosen for most analyses. For identification of minerals, spectra were collected for 5 s with three to five accumulations between 100 cm^{-1} and 3,800 cm^{-1} . For organic substances, individual spectra were collected for 10–180 s between 100 cm^{-1} and 3,800 cm^{-1} or 200 cm^{-1} and 3,800 cm^{-1} .

Formation temperatures of vein calcites were determined based on their clumped isotope (Δ_{47}) composition, which is defined as the deviation of the actual abundance of mass 47 isotopologues of CO_2 (mainly $^{18}\text{O}^{13}\text{C}^{16}\text{O}$), derived from phosphoric acid digestion of carbonates, from the abundance expected for a random distribution of isotopes (38). All clumped isotope measurements were conducted at John Hopkins University in Benjamin H. Passey's laboratory using established methods (58). Microdrilled samples were reacted in vacuo with 105% phosphoric acid held at 90 °C for 10 min. The evolved CO_2 was then cryogenically purified with dry ice/ethanol traps and a 1.2-m gas chromatography column containing Porapak Q polymer absorbent held at –20 °C. Equilibrium CO_2 prepared at 1,000 °C and 30 °C

was also analyzed concurrently to correct for instrument nonlinearity and scale compression. Measurements of NB519 and two internal carbonate standards (Carrara and 102-GC-AZ01) yield long-term average Δ_{47} values of $0.414 \pm 0.018\text{‰}$ (mean $\pm 1\sigma$ SD), $0.403 \pm 0.015\text{‰}$, and $0.710 \pm 0.015\text{‰}$, respectively (58). An acid digestion fractionation of 0.092‰ was applied to derive the clumped isotope composition of all carbonate standards and samples reported here (58). Clumped isotope temperatures were calculated using a revised temperature calibration equation based on inorganically precipitated calcites (38, 39). The oxygen isotope composition of the fluid from which these vein calcites precipitated were calculated based on the oxygen isotope composition of calcite and the clumped isotope temperatures (40). Bulk carbon and oxygen isotope compositions of the vein calcites ($\delta^{13}\text{C}_{\text{VPDB}} = -0.72 \pm 0.01\text{‰}$, $\delta^{18}\text{O}_{\text{VPDB}} = -2.46 \pm 0.06\text{‰}$) were normalized based on measurements of National Bureau of Standards, NBS-19.

The TC, organic carbon, and carbonate carbon of vein powders were analyzed using an Elementar vario Isotope cube elemental analyzer and a Multiflow-Geo headspace sampler connected to separate isotope ratio mass spectrometers (Department of Geosciences, Virginia Tech). For analysis of organic carbon, bulk rock samples were reacted with 2 N HCl to remove all acid-soluble carbon, washed with distilled H_2O , dried at 60 °C, and homogenized in an agate mortar. For inorganic carbon analyses, the samples were prepared in septum vials, flushed with He, acidified with phosphoric acid, and reacted overnight before analyses. TOC contents were calculated by mass balancing TC and TIC contents. The precision of $\delta^{13}\text{C}_{\text{TC}}$ is better than $\pm 0.13\text{‰}$ and, for $\delta^{13}\text{C}_{\text{TIC}}$, is better than $\pm 0.06\text{‰}$ and is based on repeated measurements of a range of standards [NBS-18, International Atomic Energy Agency, (IAEA)-CO1, IAEA-CO9, IAEA-CH6, IAEA-CH7]. SD of carbon contents is provided in *Carbon Geochemistry of a Suboceanic Mixing Zone* and is derived from analysis of duplicate samples to account for sample heterogeneity. SD of the isotope measurements of the duplicate samples is within the precision of the instrument.

Drill cores from ODP Leg 149, Site 897D, had been stored in a nonsterile fashion from when they were drilled in 1993 until they were subsampled in 2014. The outer surfaces were contaminated and had to be removed for lipid biomarker analysis. The inner sections were obtained from the drill core using a Buehler Isomet low-speed saw and a sterile diamond blade immersed in a sterile mixture of 70% (vol/vol) ethanol in H_2O and a 20-mM NaOH solution as the cutting fluid. The inner sections were cut and processed in a sterile laminar flow hood to reduce contamination by aerosol particles, and only sterilized equipment was used during the processing of samples. For lipid biomarker analyses, ca. 6 g of vein samples were crushed to a fine powder before three-time ultrasonic stick extraction with a dichloromethane:methanol (5:1, vol/vol) mixture. An aliquot of the combined total lipid extracts and a procedure blank was analyzed using a Dionex Ultimate 3000RS ultra-high pressure liquid chromatography system connected with a Turbolon electrospray ion source to an ABCiEX QTRAP4500 Triple Quadrupole/Ion Trap MS. Chromatographic separation of compounds was achieved with a Waters Acquity ultra performance liquid chromatography (UPLC) ethylene bridged hybrid (BEH) C18 column after Wörmer et al. (59). The tandem mass spectrometer was operated in MRM mode, Q1 and Q3 quadrupoles were set at unit mass resolution and MS conditions were optimized using commercially available standards (1,2-Di-O-hexadecyl-glycerol, Sigma Aldrich; 1,2-di-O-phytanyl-glycerol, Avanti Polar Lipids; GDGT-0 isolated from *Archaeoglobus fulgidus*). Quantification occurred in the first transition via external calibration with the available standards, and all amounts were corrected with the procedure blank.

ACKNOWLEDGMENTS. Kai-Uwe Hinrichs, who acknowledges the Gottfried Wilhelm Leibniz Program of the Deutsche Forschungsgemeinschaft (HI 616-14-1), and Benjamin H. Passey are thanked for the use of their laboratory facilities. We thank Julius S. Lipp for help with HPLC-MS analyses and provision of the GDGT-0 standard, Benjamin Gill for help with carbon isotope analyses at Virginia Tech, and Horst Marschall for providing access to scanning electron and petrographic microscopes. We used samples collected during the Ocean Drilling Program (ODP). ODP was sponsored by the US National Science Foundation and participating countries under management of Joint Oceanographic Institutions, Inc. This work was supported by The Penzance Endowed Fund in Support of Assistant Scientists (F.K. and W.G.), the Deep Ocean Exploration Institute at the Woods Hole Oceanographic Institution (F.K. and W.D.O.), and the University of Bremen (F.S.). This is Center for Dark Energy Biosphere Investigations (C-DEBI) contribution 272.

1. Sousa FL, et al. (2013) Early bioenergetic evolution. *Philos Trans R Soc Lond B Biol Sci* 368(1622):20130088.
2. Kelley DS, et al.; AT3-60 Shipboard Party (2001) An off-axis hydrothermal vent field near the Mid-Atlantic Ridge at 30 °N. *Nature* 412(6843):145–149.

3. Kelley DS, et al. (2005) A serpentinite-hosted ecosystem: The Lost City hydrothermal field. *Science* 307(5714):1428–1434.
4. Früh-Green GL, et al. (2003) 30,000 years of hydrothermal activity at the Lost City vent field. *Science* 301(5632):495–498.

5. Lang SQ, Butterfield DA, Schulte M, Kelley DS, Lilley MD (2010) Elevated concentrations of formate, acetate and dissolved organic carbon found at the Lost City hydrothermal field. *Geochim Cosmochim Acta* 74(3):941–952.
6. Proskurowski G, Lilley MD, Kelley DS, Olson EJ (2006) Low temperature volatile production at the Lost City Hydrothermal Field, evidence from a hydrogen stable isotope geothermometer. *Chem Geol* 229(4):331–343.
7. Ludwig KA, Kelley DS, Butterfield DA, Nelson BK, Früh-Green G (2006) Formation and evolution of carbonate chimneys at the Lost City Hydrothermal Field. *Geochim Cosmochim Acta* 70(14):3625–3645.
8. Brazelton WJ, Schrenk MO, Kelley DS, Baross JA (2006) Methane- and sulfur-metabolizing microbial communities dominate the Lost City hydrothermal field ecosystem. *Appl Environ Microbiol* 72(9):6257–6270.
9. Brazelton WJ, et al. (2010) Archaea and bacteria with surprising microdiversity show shifts in dominance over 1,000-year time scales in hydrothermal chimneys. *Proc Natl Acad Sci USA* 107(4):1612–1617.
10. Schrenk MO, Brazelton WJ, Lang SQ (2013) Serpentinization, carbon, and deep life. *Rev Mineral Geochem* 75(1):575–606.
11. Delacour A, Früh-Green GL, Bernasconi SM, Kelley DS (2008) Sulfur in peridotites and gabbros at Lost City (30°N, MAR): Implications for hydrothermal alteration and microbial activity during serpentinization. *Geochim Cosmochim Acta* 72(20):5090–5110.
12. Proskurowski G, et al. (2008) Abiogenic hydrocarbon production at Lost City hydrothermal field. *Science* 319(5863):604–607.
13. Lartaud F, et al. (2011) Fossil evidence for serpentinization fluids fueling chemosynthetic assemblages. *Proc Natl Acad Sci USA* 108(19):7698–7703.
14. Cox ME, Launay J, Paris JP (1982) Geochemistry of low temperature geothermal systems in New Caledonia. *Proceedings of the Pacific Geothermal Conference* (Univ Auckland, Auckland, New Zealand), pp 453–459.
15. Fryer P, et al. (1990) Conical Seamount: SeaMARC II, Alvin Submersible, and Seismic-Reflection Studies. *Proc Ocean Drill Program Initial Rep* 125:69–80.
16. Ohara Y, et al. (2012) A serpentinite-hosted ecosystem in the Southern Mariana Forearc. *Proc Natl Acad Sci USA* 109(8):2831–2835.
17. Beslier M-O, Ask M, Boillot G (1993) Ocean-continent boundary in the Iberia Abyssal Plain from multichannel seismic data. *Tectonophysics* 218(4):383–393.
18. Whitmarsh RB, Manatschal G, Minshull TA (2001) Evolution of magma-poor continental margins from rifting to seafloor spreading. *Nature* 413(6852):150–154.
19. Dean SM, Minshull TA, Whitmarsh RB, Louden KE (2000) Deep structure of the ocean-continent transition in the southern Iberia Abyssal Plain from seismic refraction profiles: The IAM-9 transect at 40°20'N. *J Geophys Res* 105(B3):5859–5885.
20. Macdonald AH, Fyfe WS (1985) Rate of serpentinization in seafloor environments. *Tectonophysics* 116(1–2):123–135.
21. Lau KWH, et al. (2006) Crustal structure across the Grand Banks—Newfoundland Basin Continental Margin—I. Results from a seismic refraction profile. *Geophys J Int* 167(1):127–156.
22. Finlayson DM, Collins CDN, Lukaszyk I, Chudyk EC (1998) A transect across Australia's southern margin in the Otway Basin region: Crustal architecture and the nature of rifting from wide-angle seismic profiling. *Tectonophysics* 288(1–4):177–189.
23. Jagoutz O, et al. (2007) The rift-to-drift transition in the North Atlantic: A stuttering start of the MORB machine? *Geology* 35(12):1087–1090.
24. Sawyer DS, Whitmarsh RB, Klaus A Shipboard Scientific Party (1994) Site 897. *Proc Ocean Drill Program Initial Rep* 149: 41–113.
25. Milliken KL, Morgan JK (1996) Chemical evidence for near-seafloor precipitation of calcite in serpentinites (Site 897) and serpentinite breccias (Site 899), Iberia Abyssal Plain. *Proc Ocean Drill Program Sci Results* 149:533–558.
26. Alt JC, Shanks WC (1998) Sulfur in serpentinized oceanic peridotites: Serpentinization processes and microbial sulfate reduction. *J Geophys Res* 103(B5):9917–9929.
27. Klein F, et al. (2014) Magnetite in seafloor serpentinite—Some like it hot. *Geology* 42(2):135–138.
28. Agrinier P, Cornen G, Beslier MO (1996) Mineralogical and oxygen isotopic features of serpentinites recovered from the ocean/continent transition in the Iberia Abyssal Plain. *Proc Ocean Drill Program Sci Results* 149:541–552.
29. Schwarzenbach EM, Früh-Green GL, Bernasconi SM, Alt JC, Plas A (2013) Serpentinization and carbon sequestration: A study of two ancient peridotite-hosted hydrothermal systems. *Chem Geol* 351:115–133.
30. Klein F, Bach W, McCollom TM (2013) Compositional controls on hydrogen generation during serpentinization of ultramafic rocks. *Lithos* 178:55–69.
31. Janeky D, Seyfried W (1986) Hydrothermal serpentinization of peridotite within oceanic crust: Experimental investigations of mineralogy and major element chemistry. *Geochim Cosmochim Acta* 50(7):1357–1378.
32. Milliken KL, Lynch FL, Seifert KE (1996) Marine weathering of serpentinites and serpentinite breccias, sites 897 and 899, Iberia Abyssal Plain. *Proc Ocean Drill Program Sci Results* 149:519–540.
33. Hardie LA (1996) Secular variation in seawater chemistry: An explanation for the coupled secular variation in the mineralogies of marine limestones and potash evaporites over the past 600 m.y. *Geology* 24(3):279–283.
34. Seyfried WE, Pester NJ, Tutolo BM, Ding K (2015) The Lost City hydrothermal system: Constraints imposed by vent fluid chemistry and reaction path models on seafloor heat and mass transfer processes. *Geochim Cosmochim Acta* 163:59–79.
35. Beard JS, Hopkinson L (2000) A fossil, serpentinization-related hydrothermal vent, Ocean Drilling Program Leg 173, Site 1068 (Iberia Abyssal Plain): Some aspects of mineral and fluid chemistry. *J Geophys Res* 105(B7):16527–16539.
36. Lang SQ, et al. (2012) Microbial utilization of abiogenic carbon and hydrogen in a serpentinite-hosted system. *Geochim Cosmochim Acta* 92:82–99.
37. Delacour A, Früh-Green GL, Bernasconi SM, Schaeffer P, Kelley DS (2008) Carbon geochemistry of serpentinites in the Lost City Hydrothermal System (30°N, MAR). *Geochim Cosmochim Acta* 72(15):3681–3702.
38. Ghosh P, et al. (2006) ¹³C-¹⁸O bonds in carbonate minerals: A new kind of paleothermometer. *Geochim Cosmochim Acta* 70(6):1439–1456.
39. Eagle RA, et al. (2013) The influence of temperature and seawater carbonate saturation state on ¹³C-¹⁸O bond ordering in bivalve mollusks. *Biogeosci Discuss* 10(7): 4591–4606.
40. Kim ST, O'Neil JR (1997) Equilibrium and nonequilibrium oxygen isotope effects in synthetic carbonates. *Geochim Cosmochim Acta* 61(16):3461–3475.
41. Amend JP, McCollom TM, Hentscher M, Bach W (2011) Catabolic and anabolic energy for chemolithoautotrophs in deep-sea hydrothermal systems hosted in different rock types. *Geochim Cosmochim Acta* 75(19):5736–5748.
42. Shank EA, et al. (2011) Interspecies interactions that result in *Bacillus subtilis* forming biofilms are mediated mainly by members of its own genus. *Proc Natl Acad Sci USA* 108(48):E1236–E1243.
43. Lutz HD, Möller H, Schmidt M (1994) Lattice vibration spectra. Part LXXXII. Brucite-type hydroxides M(OH)₂ (M = Ca, Mn, Co, Fe, Cd)—IR and Raman spectra, neutron diffraction of Fe(OH)₂. *J Mol Struct* 328:121–132.
44. Maquelin K, et al. (2002) Identification of medically relevant microorganisms by vibrational spectroscopy. *J Microbiol Methods* 51(3):255–271.
45. De Gelder J, De Gussem K, Vandebaele P, Moens L (2007) Reference database of Raman spectra of biological molecules. *J Raman Spectrosc* 38(9):1133–1147.
46. Rygula A, et al. (2013) Raman spectroscopy of proteins: A review. *J Raman Spectrosc* 44(8):1061–1076.
47. Bradley AS, Fredricks H, Hinrichs K-U, Summons RE (2009) Structural diversity of diether lipids in carbonate chimneys at the Lost City Hydrothermal Field. *Org Geochem* 40(12):1169–1178.
48. Lincoln SA, Bradley AS, Newman SA, Summons RE (2013) Archaeal and bacterial glycerol dialkyl glycerol tetraether lipids in chimneys of the Lost City Hydrothermal Field. *Org Geochem* 60:45–53.
49. Schrenk MO, Kelley DS, Bolton SA, Baross JA (2004) Low archaeal diversity linked to seafloor geochemical processes at the Lost City Hydrothermal Field, Mid-Atlantic Ridge. *Environ Microbiol* 6(10):1086–1095.
50. Pancost RD, Bouloubassi I, Aloisi G, Sinninghe Damsté JS; Medinaut Shipboard Scientific Party (2001) Three series of non-isoprenoidal dialkyl glycerol diethers in cold-seep carbonate crusts. *Org Geochem* 32(5):695–707.
51. Pons M-L, et al. (2011) Early Archean serpentine mud volcanoes at Isua, Greenland, as a niche for early life. *Proc Natl Acad Sci USA* 108(43):17639–17643.
52. Fryer P (2012) Serpentinite mud volcanism: Observations, processes, and implications. *Annu Rev Mar Sci* 4(1):345–373.
53. Cannat M, Fontaine F, Escartin J (2010) Serpentinization and associated hydrogen and methane fluxes at slow spreading ridges. *Diversity of Hydrothermal Systems on Slow Spreading Ocean Ridges*, Geophysical Monograph Series, eds Rona PA, Devoy CW, Dymet J, Murton BJ (Am Geophys Union, Washington, DC), Vol 188, pp 241–264.
54. Mével C, Stadoumi C (1996) Hydrothermal alteration of the upper mantle section at Hess Deep. *Proc Ocean Drill Program Sci Results* 147:293–309.
55. Bideau D, Hebert R, Hekinian R, Cannat M (1991) Metamorphism of deep-seated rocks from the Garrett Ultrafast Transform (East Pacific Rise near 13°25'S). *J Geophys Res* 96 (B6):10079–10099.
56. Shock EL, Schulte MD (1998) Organic synthesis during fluid mixing in hydrothermal systems. *J Geophys Res* 103(E12):28513–28527.
57. McCollom TM, Shock EL (1997) Geochemical constraints on chemolithoautotrophic metabolism by microorganisms in seafloor hydrothermal systems. *Geochim Cosmochim Acta* 61(20):4375–4391.
58. Henkes GA, et al. (2013) Carbonate clumped isotope compositions of modern marine mollusk and brachiopod shells. *Geochim Cosmochim Acta* 106:307–325.
59. Wörmer L, Lipp JS, Schröder JM, Hinrichs K-U (2013) Application of two new LC-ESI-MS methods for improved detection of intact polar lipids (IPLs) in environmental samples. *Org Geochem* 59:10–21.
60. Tucholke BE, Sibuet J-C (2007) Leg 210 synthesis: Tectonic, magmatic, and sedimentary evolution of the Newfoundland-Iberia rift. *Proc Ocean Drill Program Sci Results* 210:1–56.